

Parametric Excitation and Detection of An Electrostatic MEMS Actuator

Alaa Elhady*, Sangtak Park*, David Effa**, Eihab Abdel-Rahman*, and Mustafa Yavuz**
 Departments of *Systems Design Engineering & **Mechanical and Mechatronics Engineering,
 University of Waterloo, Waterloo, Canada

Summary. We describe a method to measure electrically out-of-plane motions of an electrostatic MEMS transducer excited parametrically via an in-plane (horizontal) electrostatic transducer. The method exploits homodyne detection of the current induced by out-of-plane motions. We present experimental results of the actuator principal parametric resonance observed using this method. The actuator possess a 1:1 internal resonance between the first in-plane and out-of-plane bending modes. A model is deployed to study the interaction between in-plane subharmonic resonance of order one-half and out-of-plane principal parametric resonance.

Introduction

Parametric excitation of Micro Electrical Mechanical Systems (MEMS) is an attractive actuation method promising a higher quality factor than direct excitation [1]. It also opens the door for out-of-plane actuation of MEMS fabricated from a single layer, such as Silicon-On-Insulator technology. Parametric resonance arises from time-dependent tuning of the system parameters, instead of direct time-dependent forcing [2]. Parametrically excited MEMS can be used for high accuracy mass sensors [3] and filters [4].

One scenario for parametric excitation is to exploit the nonlinear coupling of in-plane and out-of-plane bending modes of prismatic structures. In this work, we investigate the interaction between subharmonic and principal parametric resonances utilizing a micro beam electrostatic actuator designed to obtain a 1:1 internal resonance between the first in-plane and out-of-plane bending modes.

Actuator Design and Fabrication

The actuator, Fig. 1, is fabricated in Teledyne Dalsa's MIDIS process [5, 6] from polysilicon with density of $\rho = 2330 \text{ kg/m}^3$ and Young's modulus of $E = 169 \text{ GPa}$. Its dimensions are listed in Table 1. It comprises of a microplate supported by a cantilever beam. A bottom electrode serves as a detector of out-of-plane motions. Two sidewall electrodes provide direct (in-plane) electrostatic excitation. Note that the right sidewall electrode is removed in Fig. 1 for clarity. To avoid fabrication uncertainties, the beam width is designed slightly smaller than its thickness to guarantee that the natural frequency of out-of-plane bending will be higher than that of in-plane bending. The natural frequencies of the first in-plane and out-of-plane bending modes are then tuned to match by applying DC voltage V_{DC_B} to the bottom electrode.

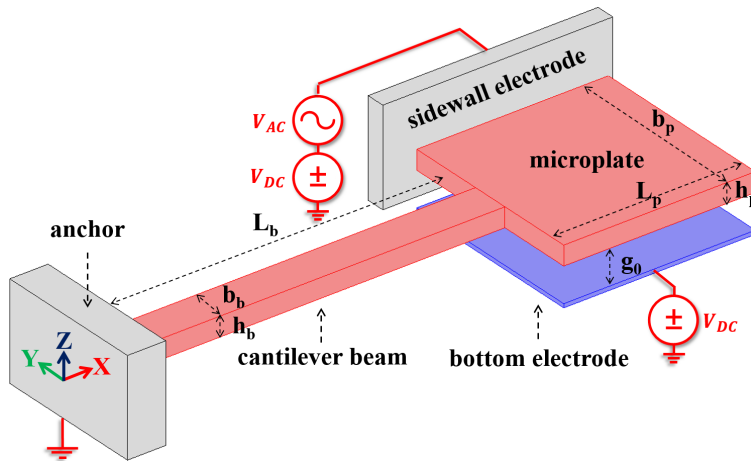


Figure 1: Schematic of the actuator

Table 1: Actuator dimensions

Parameter	Value
Beam length, L_b	400 μm
Beam width, b_b	29.5 μm
Beam thickness, h_b	30 μm
Plate length, L_p	230 μm
Plate width, b_p	215 μm
Plate thickness, h_p	30 μm
Bottom gap, d	2 μm
Side gap, g_o	2 μm

Experiment

Experimental Setup

The actuator is vacuum encapsulated in an opaque silicon cap, precluding optical motion detection. Instead, we developed a method to sense out-of-plane motions by measuring motion-induced current by a transimpedance amplifier (TIA) and detecting the frequency component of that current at the matched natural frequencies ω_n by a lock-in amplifier (LIA). Figure 2 shows the equivalent circuit of the actuator and the motion detection circuit.

The microplate is excited in-plane (along the Y-axis) at twice the natural frequency $\Omega = 2\omega_n$ and the current flowing through the bottom electrode is collected. The LIA is set to lock onto the second harmonic $2\omega_n$ in order to detect resonant motions at ω_n . This current therefore serves as a detector for resonant out-of-plane motions with a frequency of ω_n .

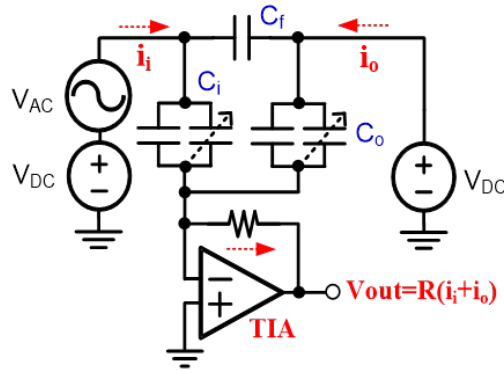


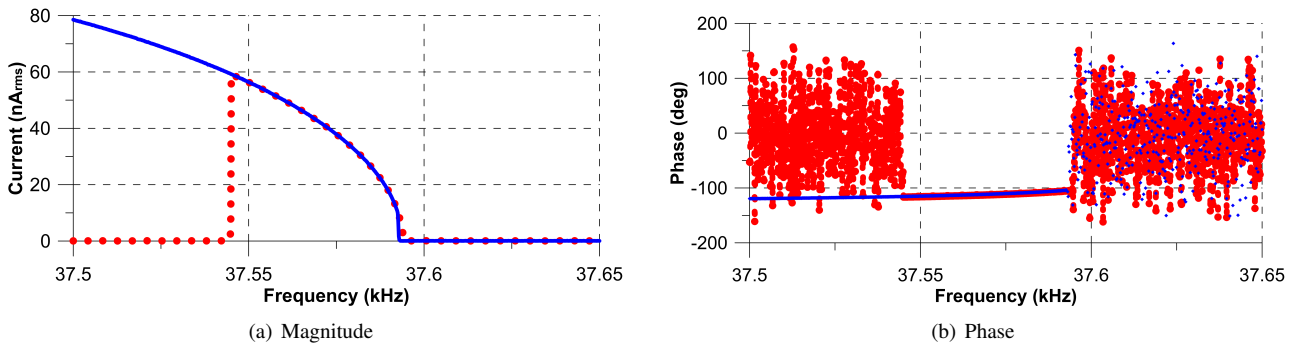
Figure 2: Circuit model for the actuator

The microplate is connected to virtual ground through TIA, while the bottom electrode is connected to a DC voltage source set to $V_{DC_B} = 37.5$ V. One of the sidewall electrodes is connected to an arbitrary waveform generator that provides the direct excitation signal, while the other sidewall electrode is grounded. The forcing frequency is varied in a frequency range $\Omega = [75 - 75.3]$ kHz $\approx 2\omega_n$.

$$v(t) = V_{DC_S} + V_{AC_S} \sin(\Omega t) \quad (1)$$

Experimental Results

The primary motion of the microplate occurs in-plane. No motion is observed out-of-plane (along the Z-axis) below the activation level of parametric resonance. Beyond the activation level, resonant out-of-plane motions are measured by the TIA in the vicinity of ω_n . The magnitude and phase frequency-response curves of the out-of-plane motion are shown in Fig. 3 for $V_{DC_S} = 60$ V and $V_{AC_S} = 30$ V. They demonstrate classical principal parametric characteristics: a sudden jump-up from a trivial response to a non-trivial response during frequency sweep-up (red dots) and a hysteretic jump-down to the trivial response during frequency sweep-down (blue dots). The corresponding phase frequency-response curve, Fig. 3(b), shows a deterministic slowly-varying phase delay of the the out-of-plane response with respect to in-plane excitation and within the principal parametric resonance window of instability. Outside of this window, the phase of the nontrivial response obtained in frequency down-sweep is deterministic while the phase delay of the trivial responses is stochastic


 Figure 3: Frequency-response of the out-of-plane motion for $V_{ac} = 30$ V and $V_S = 60$ V

Model

Analytical Model

To study the interaction between in-plane $v(x, t)$ and out-of-plane $w(x, t)$ motions, we follow Kambali and Pandey [7] to extract a reduced-order model (ROM) of the actuator. The model describes the support beam motions taking into account viscous damping, beam in-extensibility, in-plane, and out-of-plane electrostatic forces

$$\begin{aligned} \rho A \ddot{v} + c_s \dot{v} + EI_z v^{iv} - \frac{EA}{2L_b} v'' \int_0^{L_b} (w'^2 + v'^2) dx &= 0 \\ \rho A \ddot{w} + c_b \dot{w} + EI_y w^{iv} - \frac{EA}{2L_b} w'' \int_0^{L_b} (w'^2 + v'^2) dx &= 0 \end{aligned} \quad (2)$$

where A is the beam's cross-sections area, c_s and c_b are the viscous damping coefficients for in-plane and out-of-plane motions, respectively, and I_z and I_y are the beam second-moment of area around the Y- and Z-axes, respectively. The

forces and moments acting on the microplate, with mass M_p , appear as boundary conditions at the beam tip ($x = L_b$):

$$\begin{aligned}
 F_z &= -M_p \ddot{w}(L_b, t) + \frac{\epsilon L_p b_p V_{DCB}^2}{2(d - w(L_b, t))(d - w(L_b, t) - L_p w'(L_b, t))} \\
 M_y &= -\frac{M_p L_p^2}{3} \ddot{w}'(L_b, t) + \frac{\epsilon L_p^2 b_p V_{DCB}^2}{4(d - w(L_b, t))(d - w(L_b, t) - L_p w'(L_b, t))} \\
 F_y &= -M_p \ddot{v}(L_b, t) + \frac{\epsilon L_p h_p (V_{DCS} + V_{ACS})^2}{2(g_o - v(L_b, t))(g_o - v(L_b, t) - L_p v'(L_b, t))} \\
 M_z &= -\frac{M_p L_p^2}{3} \ddot{v}'(L_b, t) + \frac{\epsilon L_p^2 h_p (V_{DCS} + V_{ACS})^2}{4(g_o - v(L_b, t))(g_o - v(L_b, t) - L_p v'(L_b, t))}
 \end{aligned} \tag{3}$$

They comprise of account for the inertia of the plate and the electrostatic force and moment acting on the plate. These partial differential equations of motion were nondimensionalized with respect to L_b , g_o , d , and the time-scale $T = \sqrt{\frac{12\rho L_b^4}{b_b^2 E}}$. The nondimensional equations are:

$$\begin{aligned}
 \ddot{v} + c_s \dot{v} + v^{iv} - v'' \int_0^1 (\alpha_1 v'^2 + \alpha_2 w'^2) dx &= 0 \\
 \alpha_3 \ddot{w} + c_b \dot{w} + w^{iv} - \alpha_3 w'' \int_0^1 (\alpha_1 v'^2 + \alpha_2 w'^2) dx &= 0
 \end{aligned} \tag{4}$$

where the parameters α_1 , α_2 , α_3 , c_b , and c_s are defined in appendix A.

To reduce those equations of motion into ordinary differential equations, we use Galerkin expansion in terms of the first in-plane and out-of-plane bending mode shapes $\phi(x)$:

$$\begin{aligned}
 v(x, t) &= \phi(x)q(t) \\
 w(x, t) &= \phi(x)p(t)
 \end{aligned} \tag{5}$$

Towards that end, we multiply the equations of motion, Eqs. (4), by the mode shape $\phi(x)$ and integrate over the domain:

$$\begin{aligned}
 \int_0^1 \phi(x) \left[\ddot{v} + c_s \dot{v} + v^{iv} - v'' \int_0^1 (\alpha_1 v'^2 + \alpha_2 w'^2) dx \right] dx &= 0 \\
 \int_0^1 \phi(x) \left[\alpha_3 \ddot{w} + c_b \dot{w} + w^{iv} - \alpha_3 w'' \int_0^1 (\alpha_1 v'^2 + \alpha_2 w'^2) dx \right] dx &= 0
 \end{aligned} \tag{6}$$

We account for the boundary conditions, by applying integration by-parts to the fourth-order terms in Eqs. (6), as follows:

$$\begin{aligned}
 \int_0^1 \phi(x) w^{iv}(x, t) dx &= \phi(x) w'''(x, t) \Big|_0^1 - \int_0^1 \phi'(x) w'''(x, t) dx \\
 &= \phi(x) w'''(x, t) \Big|_0^1 - \phi'(x) w''(x, t) \Big|_0^1 + \int_0^1 \phi''(x) w''(x, t) dx
 \end{aligned} \tag{7}$$

The boundary conditions can then be substituted into Eq. (7) to yield,

$$\begin{aligned}
 \int_0^1 \phi(1) w^{iv}(x, t) dx &= \phi(1) w'''(1, t) - \phi'(1) w''(1, t) + \int_0^1 \phi''(x) w''(x, t) dx \\
 &= -F_z \phi(1) + M_y \phi'(1) + \int_0^1 \phi''(x) w''(x, t) dx
 \end{aligned} \tag{8}$$

where F_z and M_y are the total force and moment at the beam end given in the nondimensional form by:

$$\begin{aligned}
 F_z &= -\eta_{w1} \ddot{w}(1, t) + \eta_{w2} \frac{V_{DCB}^2}{(1 - w(1, t))(1 - w(1, t) - \frac{L_p}{L_b} w'(1, t))} \\
 M_y &= -\eta_{w3} \ddot{w}'(1, t) + \eta_{w4} \frac{V_{DCB}^2}{(1 - w(1, t))(1 - w(1, t) - \frac{L_p}{L_b} w'(1, t))}
 \end{aligned} \tag{9}$$

where the parameters η_{ij} are defined in appendix A.

A similar procedure is applied to the in-plane displacement $v(x, t)$, the result is substituted into (6) before carrying out the Galerkin expansion on those equations to obtain a set of two ordinary differential equations representing the reduced-order model:

$$\begin{aligned} \beta_4 \ddot{q} + \beta_5 \dot{q} + \beta_6 q + \beta_7 q^3 + \beta_8 p^2 q &= \frac{\beta_1 V_{DC_B}^2}{(1 - \beta_2 q)(1 - \beta_3 q)} \\ \beta_4 \ddot{p} + \beta_5 \gamma_4 \dot{p} + \beta_6 p + \beta_7 p^3 + \beta_8 p q^2 &= \beta_1 \frac{\gamma_1 V_{DC_S}^2 - \gamma_2 V_{AC_S} V_{DC_S} \cos(\Omega t) - \gamma_3 V_{AC_S}^2 \cos^2(\Omega t)}{(1 - \beta_2 p)(1 - \beta_3 p)} \end{aligned} \quad (10)$$

Numerical Results

To identify the actuator parameters, the model predicted out-of-plane pull-in voltage and natural frequency were matched to those measured experimentally. The measured pull in voltage was 54 Volts and the natural frequency was $\omega_n = 46$ kHz. This parameter identification routine resulted in adjusting the device layer thickness to $h_b = h_p = 28 \mu\text{m}$, the beam width to $b_b = 28 \mu\text{m}$, and the bottom gap to $d = 2.4 \mu\text{m}$. All of these dimensions are within the standard tolerances of the fabrication technology. The static pull-in voltage obtained from solving Eqs. (4) numerically with the adjusted dimensions was 53.1 V.

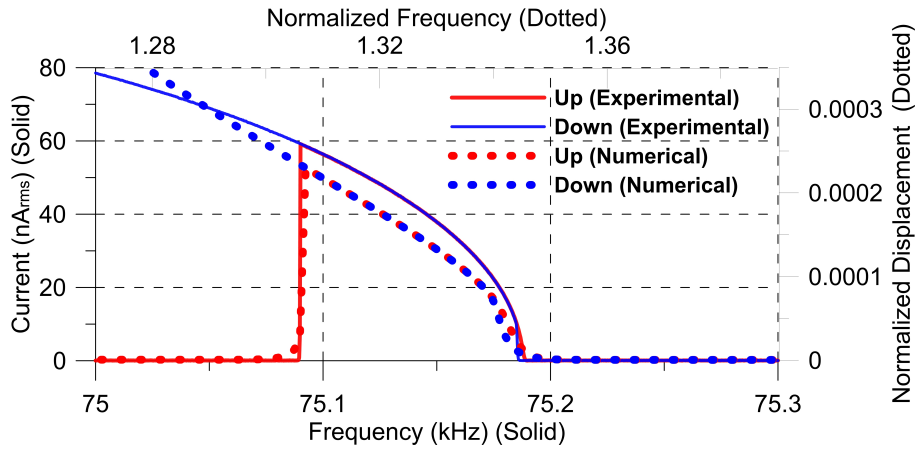


Figure 4: Experimentally measured and numerically predicted frequency-response curves for $V_{DC_B} = 37.5$ V, $V_{DC_S} = 60$ V and $V_{AC_S} = 30$ V

The quality factor of out-of-plane motions was measured experimentally as $Q = 10$. Using the identified dimensions and properties listed above, the equations of motion, Eqs. (10), were integrated numerically for 300 excitation periods τ to obtain the steady-state response. Figure 4 shows the frequency-response curve for the normalized out-of-plane peak-to-peak displacement where the bottom electrode voltage is set to $V_{DC_B} = 37.5$ V and the sidewall electrode bias and signal amplitude are set to $V_{DC_S} = 60$ V and $V_{AC_S} = 30$ V. The nondimensional natural frequency of the first out-of-plane bending mode under this waveform was $\omega_n = 0.72$. The frequency up-sweep is shown in red dots while the down-sweep is shown in blue dots. The experimentally measured frequency response curves are shown in solid red lines, for the up-sweep, and blue lines, for the down-sweep. The two frequency-response curves are in good agreement, thereby validating the model. They demonstrate a window of instability in the frequency range [75.09, 75.19] kHz, corresponding to $\Omega \approx 2\omega_n$, and co-existence of the trivial and for the non-trivial responses in a frequency range below 75.09 kHz.

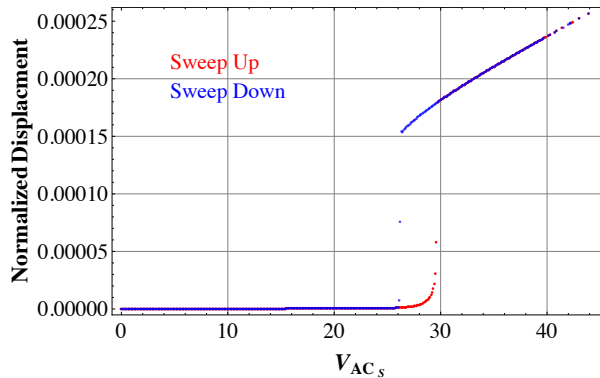


Figure 5: The out-of-plane force-response curve for $V_{DC_B} = 37.5$ V, $V_{DC_S} = 60$ V and $\Omega = 1.31$

The force-response was obtained to determine the actuator's activation level, where the non-trivial response first appears. Figure 5 shows a force sweep of V_{AC_S} where the bias voltages were set to $V_{DC_B} = 37.5$ V and $V_{DC_S} = 60$ and the signal frequency was set to $\Omega = 1.31$. The activation level under these conditions was found to be $V_{AC_S} = 29.2$ V corresponding to the Hopf bifurcation encountered along the branch of trivial solutions during force up-sweep. The window of instability was mapped by repeating this analysis at different signal frequencies Ω to obtain the instability plot shown in Fig. 6. The shaded area in the figure indicate the region in the forcing parameter space where principal parametric resonance is realizable. The minimum activation level was found to be $V_{AC_S} = 20$ V at a signal frequency of $\Omega = 1.329$.

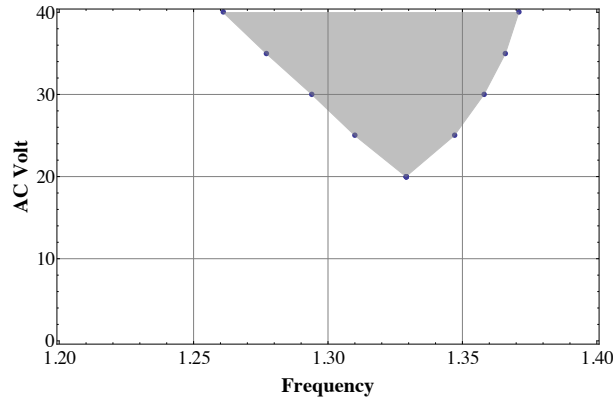


Figure 6: The instability plot of principal parametric resonance for $V_{DC_B} = 37.5$ V, $V_{DC_S} = 60$, and $Q = 10$

The model was used to investigate the effect of mistuning on energy transfer between in-plane subharmonic resonance and out-of-plane principal parametric resonance. The bottom electrode bias voltage V_{DC_B} was used to tune the initially mis-tuned natural frequency of the out-of-plane bending mode while the in-plane mode was excited with the waveform $V_{DC_S} = 60$, $V_{AC_S} = 30$. As the magnitude of V_{DC_B} was varied from 20 V to 42 V in discrete steps, a frequency sweep was undertaken at each step to determine the resonant peak-to-peak out-of-plane displacement. These values are plotted in Fig.7 as a function of V_{DC_B} . The maximum resonant displacement is obtained at $V_{DC_B} = 30.6$ V where the in-plane and out-of-plane natural frequencies are tuned. It is obvious that tuning the two natural frequencies enhances the energy transfer channel between the two modes, thus amplifying principal parametric resonance.

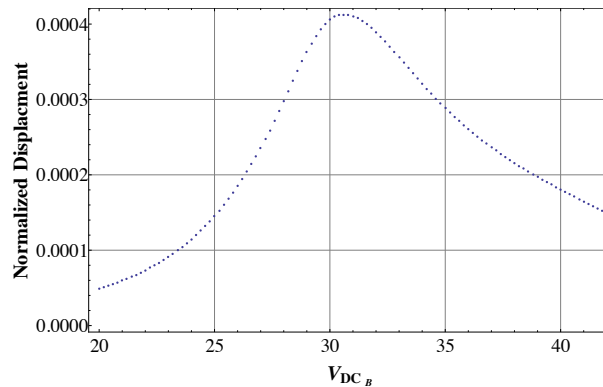


Figure 7: The peak-to-peak out-of-plane displacement as a function of the the bottom electrode bias voltage V_{DC_B}

Conclusions

This paper presented experimental evidence of in-plane subharmonic resonance of order one-half and measurements of out-of-plane principal parametric resonance. To our knowledge, this is the first all-electric implementation of parametric resonance where both excitation and detection have been achieved via electrostatic transducers. We also developed a model that captures the interaction between the actuator's in-plane and out-of-plane motions and validated it by comparison to experimental results. The model was then utilized to examine the activation level of principal parametric resonance, the region in the forcing parameter-space where it results in nontrivial response, and the relationship between in-plane and out-of-plane natural frequency mistuning and energy transfer between the corresponding resonances. As expected, we found that reducing modal mistuning enhances energy transfer from in-plane subharmonic resonance to out-of-plane principal parametric resonance.

References

- [1] Mahboob I., Yamaguchi H. (2008) Piezoelectrically Pumped Parametric Amplification and Q Enhancement in an Electromechanical Oscillator. *Applied Physics Letters* **92**:173109.
- [2] Turner K.L., Miller S.A., Hartwell P.G., MacDonald N.C., Strogatz S.H., Adams S.G. (1998) Five Parametric Resonances in a Microelectromechanical System. *Nature* **396**:149-52.
- [3] Zhang W, Turner KL. A mass sensor based on parametric resonance. In *Proceedings of the Solid State Sensor, Actuator and Microsystem Workshop*, Hilton Head Island, SC 2004 Jun 6 (pp. 49-52).
- [4] Shaw SW, Turner KL, Rhoads JF, Baskaran R. Parametrically excited MEMS-based filters. In *IUTAM Symposium on Chaotic Dynamics and Control of Systems and Processes in Mechanics 2005* (pp. 137-146). Springer Netherlands.
- [5] MEMS Integrated Design for Inertial Sensors (MIDIS). [Online]. Available: <http://www.teledynedalsa.com/semi/mems/applications/midis/>, accessed Jul. 16, 2015.
- [6] A. Merdassi, P. Yang, and V. P. Chodavarapu, "A wafer level vacuum encapsulated capacitive accelerometer fabricated in an unmodified commercial MEMS process," *Sensors*, vol. 15, no. 4, pp. 7349-7359, 2015.
- [7] Kambali PN, Pandey AK. Nonlinear coupling of transverse modes of a fixed-fixed microbeam under direct and parametric excitation. *Nonlinear Dynamics*. 2017 Jan 1;87(2):1271-94.

Appendix A - Lumped Parameters

$$\begin{aligned}
 \alpha_1 &= \frac{6g_o^2}{b_b^2} & \alpha_2 &= \frac{6d^2}{b_b^2} & \alpha_3 &= \frac{b_b^2}{h_b^2} \\
 c_b &= \frac{2\sqrt{3}L_b^2 C_b}{h_b^3 \sqrt{E\rho}} & & & c_s &= \frac{2\sqrt{3}L_b^2 C_s}{b^2 h_b \sqrt{E\rho}} \\
 \eta_{w1} &= \frac{b_b b_p h_p L_p}{h_b^3 L_b} & & & \eta_{w2} &= -\frac{6b_p L_b^3 L_p \epsilon}{b_b d^3 E h_b^3} \\
 \eta_{w3} &= -\frac{b_b b_p h_p L_p^3}{3h_b^3 L_b^3} & & & \eta_{w4} &= \frac{3b_p L_b^2 L_p^2 \epsilon}{b_b d^3 E h_b^3} \\
 \eta_{v1} &= \frac{b_p h_p L_p}{b_b h_b L_b} & & & \eta_{v2} &= -\frac{6h_p L_b^3 L_p \epsilon}{b_b^3 E g_o^3 h_b} \\
 \eta_{v3} &= -\frac{b_p h_p L_p^3}{3b_b h_b L_b^3} & & & \eta_{v4} &= \frac{3h_p L_b^2 L_p^2 \epsilon}{b_b^3 E g_o^3 h_b}
 \end{aligned}$$